Drag, lift and torque correlations for non-spherical particles from Stokes limit to high Reynolds numbers

Pacha Sanjeevi, Sathish; Kuipers, J. A.M.; Padding, Johan T.

DOI
10.1016/j.ijmultiphaseflow.2018.05.011

Publication date
2018

Document Version
Accepted author manuscript

Published in
International Journal of Multiphase Flow

Drag, lift and torque correlations for non-spherical particles from Stokes limit to high Reynolds numbers

Sathish K. P. Sanjeevi[a], J. A. M. Kuipers[b], Johan T. Padding[a,*]

[a] *Process and Energy Department, Delft University of Technology, Leeghwaterstraat 39, 2628 CB Delft, The Netherlands*

[b] *Department of Chemical Engineering and Chemistry, Eindhoven University of Technology, 5600 MB Eindhoven, The Netherlands*

Abstract

Accurate direct numerical simulations are performed to determine the drag, lift and torque coefficients of non-spherical particles. The numerical simulations are performed using the lattice Boltzmann method with multi-relaxation time. The motivation for this work is the need for accurate drag, lift and torque correlations for high Re regimes, which are encountered in Euler-Lagrangian simulations of fluidization and pneumatic conveying of larger non-spherical particles. The simulations are performed in the Reynolds number range $0.1 \leq Re \leq 2000$ for different incident angles ϕ. Different tests are performed to analyse the influence of grid resolution and confinement effects for different Re. The measured drag, lift and torque coefficients are utilized to derive accurate correlations for specific non-spherical particle shapes, which can be used in unresolved simulations. The functional forms for the correlations are chosen to agree with the expected physics at Stokes flow as well as the observed leveling off of the drag coefficient at high Re flows. Therefore the fits can be extended to regimes outside the Re regimes simulated. We observe sine-squared scaling of the drag coefficient for the particles tested even at $Re = 2000$ with $C_{D,\phi} = C_{D,\phi=0^\circ} + (C_{D,\phi=90^\circ} - C_{D,\phi=0^\circ}) \sin^2 \phi$. Furthermore, we also observe that the lift coefficient approximately scales as $C_{L,\phi} = (C_{D,\phi=90^\circ} - C_{D,\phi=0^\circ}) \sin \phi \cos \phi$ for the elongated particles. The current work would greatly improve the accuracy of Euler-Lagrangian simulations of larger non-spherical particles considering the existing literature is mainly limited to steady flow regimes and lower Re.

*J.T.Padding@tudelft.nl

Keywords: Non-spherical particles, Force and torque correlation, Lattice Boltzmann method.

1. Introduction

Particulate suspensions are involved in different natural and man-made processes. Examples are red blood cells in plasma, fluidization of pulverized coal and milled biomass, and fibrous pulps in the paper manufacturing industry, etc. Traditionally, particulate suspension studies simplify the particles as spheres (Ladd, 1994a,b; Ladd and Verberg, 2001; Beetstra et al., 2007), thereby eliminating orientation and shape effects. In general, simplifying non-spherical particles with an equivalent sphere can provide an approximate drag prediction, but the effects of lift and torque and also their dependence with orientation are often ignored. The spherical particle approximation for applications like fluidized beds with non-spherical particles could significantly influence the minimum fluidization velocity, power consumption and also affect the overall bed dynamics (Hilton et al., 2010). Therefore, quantification of the effects of particle orientation on drag, lift and torque is important.

In the Stokes limit, theoretical investigations are available for different non-spherical particles. Oberbeck (1876) derived the drag for translation of a spheroid parallel to its principal axis. Jeffery (1922) studied the motion of an ellipsoid in shear flow. He suggested that the ellipsoidal particle translates in a way corresponding to least dissipation of energy, and that the final state depends on the initial state of the particle. Several empirical drag correlations have been proposed in the past for isolated non-spherical particles as a function of the Reynolds number Re. Leith (1987) extended Stokes' law for a sphere to arbitrary non-spherical objects by decomposing the pressure and viscous components and accordingly using the object's projected area and surface area, respectively, to represent the total drag.

Haider and Levenspiel (1989) proposed a drag correlation for arbitrary particles as a function of sphericity, but not considering the orientation. Ganser (1993) compiled experimental data of several non-spherical shapes and proposed a drag correlation as a function of two shape factors, namely Stokes' and Newton's shape factors. Recently, Hölzer and Sommerfeld (2008) proposed a drag correlation based on a large set of numerical and experimental data, involving two different projected areas to account for particle orientation. Hölzer and Sommerfeld (2009) and Zastawny et al. (2012) investigated different non-spherical particles at different flow incident angles ϕ and

Re, albeit limiting mainly to the steady flow regime. Richter and Nikrityuk (2012, 2013) simulated heat transfer and drag of an ellipsoid and a cube. Very recently, Ouchene et al. (2016) proposed force and torque correlations for prolate spheroids, applicable to a range of aspect ratios up to 32. Their work was limited to steady flows with $Re \leq 240$.

Zastawny et al. (2012) provide correlations for drag, lift and torque based on immersed boundary direct numerical simulations (DNS). Their particle's equivalent volume sphere diameters (d_{eq}) range between 8 to 12 grid cells for Re from 0.1 upto 300. However, their work does not provide a detailed study on the influence of grid resolution as function of Re. Even their highest resolution of $d_{eq} = 12$ implies that the critical minimum thickness would be of the order of a few cells for high aspect ratio disk and a fibre of aspect ratio 5. In our current work, detailed studies on grid resolution and wall confinement effects are performed for different Re. We also observe that the Zastawny et al. (2012) results are not accurate at Stokes flow, but improve at larger Re. Similar deviations in the results of Zastawny et al. (2012) have also been observed by Ouchene et al. (2015, 2016).

Some authors define the Reynolds number Re_d based on the minimum thickness of the particle d_{min}. For this work, the Reynolds number is defined as

$$Re = |\boldsymbol{u}_\infty| d_{eq}/\nu, \tag{1}$$

where $\boldsymbol{u}_\infty$ is the uniform inlet velocity, d_{eq} is the diameter of the volume-equivalent sphere, and ν is the kinematic viscosity of the fluid. The drag, lift and torque coefficients respectively are defined as

$$C_D = |\boldsymbol{F}_D|/(\frac{1}{2}\rho_f |\boldsymbol{u}_\infty|^2 \frac{\pi}{4} d_{eq}^2), \tag{2}$$

$$C_L = |\boldsymbol{F}_L|/(\frac{1}{2}\rho_f |\boldsymbol{u}_\infty|^2 \frac{\pi}{4} d_{eq}^2), \text{ and} \tag{3}$$

$$C_T = |\boldsymbol{T}|/(\frac{1}{2}\rho_f |\boldsymbol{u}_\infty|^2 \frac{\pi}{8} d_{eq}^3). \tag{4}$$

Here, $\boldsymbol{F}_D, \boldsymbol{F}_L$ and $\boldsymbol{T}$ are drag, lift, and pitching torque acting on the particle, and ρ_f is the fluid density.

The motivation for this work is the need for highly accurate C_D, C_L, and C_T correlations for high Re regimes, which are encountered in Euler-Lagrangian simulations of fluidization and pneumatic conveying of larger

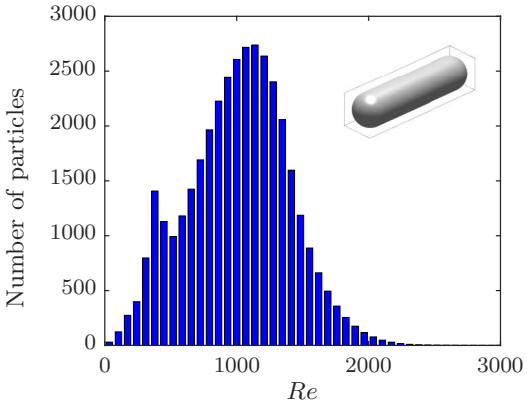

Figure 1: Time-averaged distribution of particle Re from Euler-Lagrangian fluidization simulations of spherocylindrical particles of aspect ratio 4 (inset).

non-spherical particles. We performed such simulations of spherocylindrical (biomass-like, type Geldart D) particles of aspect ratio 4, using the Hölzer and Sommerfeld (2008) drag correlation with Di Felice (1994) voidage correction. The resulting distribution of particle Re encountered during the simulation is plotted in figure 1. It can be observed that the median of the distribution is around $Re \approx 1200$ and the maximum is around $Re \approx 2000$. For this Re range, we perform fully resolved simulations of the fluid flow around the particles using the lattice Boltzmann method (LBM) and suitably parametrize the simulation data to obtain the C_D, C_L, and C_T correlations.

The work of Rubinstein et al. (2017) (in their figure 2) shows that fixed particle simulations are sufficient to compute forces in moving particulate systems, provided the Stokes number (St) is sufficiently high, around $St \geq 10$. The Stokes number is the measure of timescales of the particle against the fluid. The relation between St and Re is given by $St = (\rho_p/(18\rho_f))Re$, where ρ_p is the particle density. The above relationship is of order $St = 50Re$ for gas-solid systems (assuming a typical value of ρ_p/ρ_f of 10^3) and therefore generally results in very large Stokes numbers. Therefore, in gas-solid fluidization and other typical engineering applications such as pneumatic conveying, riser flows, etc., a quasi-steady particle orientation assumption can be applied for Euler-Lagrangian simulations.

The simulated non-spherical particles are shown in figure 2. LBM simulations for high Re flows have been performed in the past. Eitel-Amor et al. (2013) performed detailed simulations of flow past a sphere in the

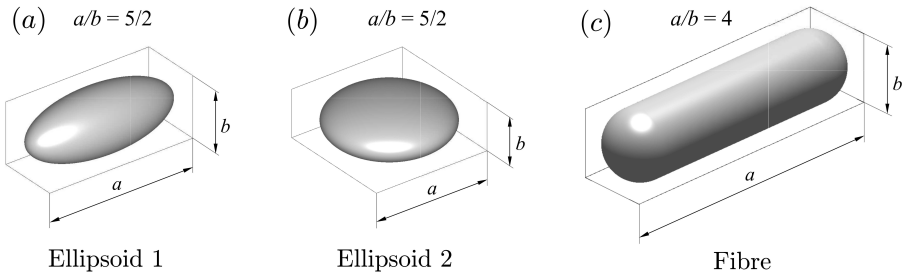

Figure 2: Different non-spherical particles simulated in this work: (a) Ellipsoid 1 - a prolate spheroid of aspect ratio 5/2, (b) Ellipsoid 2 - an oblate spheroid of aspect ratio 5/2, and (c) Fibre - a spherocylinder of aspect ratio 4.

laminar regime of $100 \leq Re \leq 300$ and sub-critical turbulent flow regime $3700 \leq Re \leq 10000$ using a single-relaxation scheme (SRT) with hierarchical grid refinement. In this work, we use a multi-relaxation time (MRT) LBM scheme, which adds stability required for the high Re simulations. Kruggel-Emden et al. (2016) provide a good overview of coupled fluid flow and heat transfer simulations for particulate flows using LBM.

For Stokes flow (Happel and Brenner, 1983), C_D and C_L at different incident angle ϕ are given by

$$C_{D,\phi} = C_{D,\phi=0^\circ} + (C_{D,\phi=90^\circ} - C_{D,\phi=0^\circ}) \sin^2 \phi, \tag{5}$$

$$C_{L,\phi} = (C_{D,\phi=90^\circ} - C_{D,\phi=0^\circ}) \sin \phi \cos \phi. \tag{6}$$

Interestingly, for all the investigated particles, C_D scales as a *sine-squared* function as in equation 5, even for Reynolds numbers as high as 2000. Further, C_L also scales as $\sin \phi \cos \phi$ as in equation 6, for the *elongated* particles even at $Re = 2000$. Equations 5 and 6 arise from the linearity of the Navier-Stokes equations in the Stokes regime. We have investigated these scaling phenomena in detail for high Re (Sanjeevi and Padding, 2017). However, we found that the real cause is due to the dependency of pressure on the local surface normal's orientation with the incoming flow and not due to the flow linearity as in Stokes flow.

To the best of our knowledge, the present work is the only work that in detail investigates different non-spherical particles upto high Reynolds numbers of $Re = 2000$ for different incident angles $0^\circ \leq \phi \leq 90^\circ$. There have been similar works providing C_D, C_L, and C_T correlations as a function of Re and ϕ (Zastawny et al., 2012; Richter and Nikrityuk, 2013; Ouchene et al.,

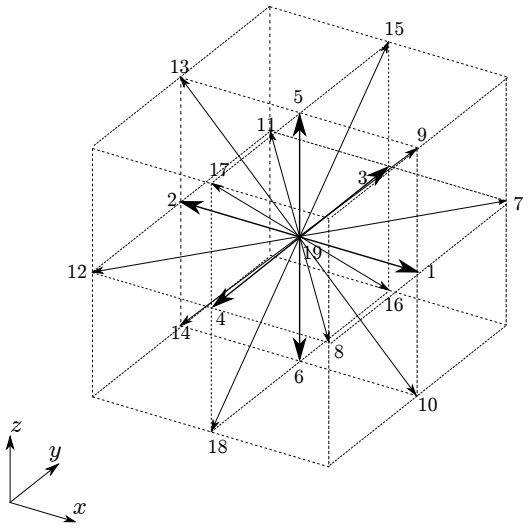

Figure 3: D3Q19 lattice configuration with directions α.

2016), but our work considers approximately an order of magnitude larger Re than these studies. By extending the measurements to larger flow velocities, our correlations take into account the leveling off of the drag coefficient observed at higher Re. Note that our work does not aim to give a generic correlation for *all* particle shapes and/or aspect ratios. Rather, by defining separate correlation functions for each specific particle shape and aspect ratio, we are able to derive more accurate correlation functions for the chosen particle shapes.

This work will be helpful for the community dealing with Euler-Lagrangian simulations of non-spherical particles, for practical industrial applications such as biomass fluidization, pneumatic conveying and riser flows of non-spherical particles.

2. Numerical method

2.1. Lattice Boltzmann method

The flow is simulated using the D3Q19 multi-relaxation time (MRT) lattice Boltzmann method (d'Humières et al., 2002). The MRT-LBM scheme solves the evolution of particle distribution function $|f\rangle$

$$|f(\boldsymbol{r}+\boldsymbol{e}_\alpha\Delta t, t+\Delta t)\rangle = |f(\boldsymbol{r},t)\rangle - \boldsymbol{M}^{-1}\hat{\boldsymbol{S}}(|m(\boldsymbol{r},t)\rangle - |m^{(eq)}(\boldsymbol{r},t)\rangle), \quad (7)$$

at position $\boldsymbol{r}$ with discrete velocities $\boldsymbol{e}_\alpha$ in directions $\alpha = 1, 2..., 19$ as shown in figure 3. $\boldsymbol{M}$ is a 19×19 transformation matrix (see Appendix A) used to transform $|f\rangle$ from velocity space to moment space $|m\rangle$ with $|m\rangle = \boldsymbol{M} \cdot |f\rangle$. Here, the ket vector $|\cdot\rangle$ implies a column vector. The relaxation matrix $\hat{\boldsymbol{S}} = \boldsymbol{M} \cdot \boldsymbol{S} \cdot \boldsymbol{M}^{-1}$ is a 19×19 diagonal matrix. The LBM simulations are performed in lattice units and the lattice speed is $c = \Delta x/\Delta t$ with $\Delta x = 1$ and $\Delta t = 1$. The lattice speed of sound is $c_s = c/\sqrt{3}$. For the D3Q19 model, the 19 moments are

$$|m\rangle = (\rho, e, \epsilon, j_x, q_x, j_y, q_y, j_z, q_z, 3p_{xx}, 3\pi_{xx}, p_{ww}, \pi_{ww}, p_{xy}, p_{yz}, p_{zx}, m_x, m_y, m_z)^T, \tag{8}$$

where density $\rho = \sum_\alpha f_\alpha$ and momentum $\boldsymbol{j} = (j_x, j_y, j_z) = \rho \boldsymbol{u} = \sum_\alpha f_\alpha e_\alpha$ are the conserved moments. The non-conserved moments are as follows: e is the part of kinetic energy independent of density, ϵ is the part of kinetic energy squared independent of both the density and kinetic energy ($\epsilon = e^2$), and q_i is the energy flux independent of mass flux (d'Humières et al., 2002). Here, subscript i denotes x, y, or z-coordinates. $p_{xx}, p_{xy}, p_{yz}, p_{xz}$ and p_{ww} are the symmetric traceless viscous stress tensor with $p_{ww} = p_{yy} - p_{zz}$ and $p_{xx} + p_{yy} + p_{zz} = 0$. m_x, m_y and m_z are the third order moments. π_{xx} and π_{ww} are fourth order moments. The equilibria of non-conserved moments are given as functions of ρ and $\boldsymbol{j}$ (d'Humières et al., 2002) as

$$e^{(eq)} = -11\rho + \frac{19}{\rho_0}\boldsymbol{j} \cdot \boldsymbol{j} = -11\rho + \frac{19}{\rho_0}(j_x^2 + j_y^2 + j_z^2), \tag{9}$$

$$\epsilon^{(eq)} = w_\epsilon \rho + \frac{w_{\epsilon j}}{\rho_0}\boldsymbol{j} \cdot \boldsymbol{j}, \tag{10}$$

$$q_x^{(eq)} = -\frac{2}{3}j_x, \quad q_y^{(eq)} = -\frac{2}{3}j_y, \quad q_z^{(eq)} = -\frac{2}{3}j_z, \tag{11}$$

$$p_{xx}^{(eq)} = \frac{1}{3\rho_0}(2j_x^2 - (j_y^2 + j_z^2)), \quad p_{ww}^{(eq)} = \frac{1}{\rho_0}(j_y^2 - j_z^2), \tag{12}$$

$$p_{xy}^{(eq)} = \frac{1}{\rho_0}j_x j_y, \quad p_{yz}^{(eq)} = \frac{1}{\rho_0}j_y j_z, \quad p_{xz}^{(eq)} = \frac{1}{\rho_0}j_x j_z, \tag{13}$$

$$\pi_{xx}^{(eq)} = w_{xx} p_{xx}^{(eq)}, \quad \pi_{ww}^{(eq)} = w_{xx} p_{ww}^{(eq)}, \tag{14}$$

$$m_x^{(eq)} = m_y^{(eq)} = m_z^{(eq)} = 0, \tag{15}$$

where ρ_0 is the average density in the system. In our simulations, $\rho_0 = 1$, $w_\epsilon = 3, w_{\epsilon j} = -11/2$, and $w_{xx} = -1/2$. The factor $1/\rho_0$ used in the above equilibrium expressions is to reduce compressibility effects (He and Luo, 1997;

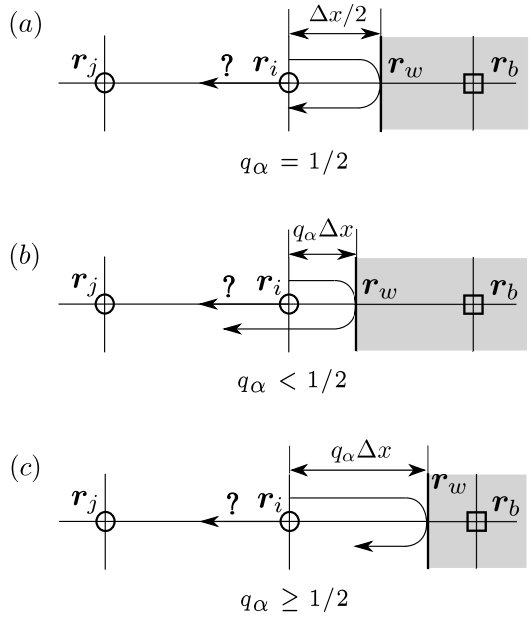

Figure 4: The linearly interpolated bounce-back scheme simplified in one-dimension.

d'Humières et al., 2002). The diagonal collision matrix $\hat{\boldsymbol{S}}$ (d'Humières et al., 2002; Huang et al., 2012) is

$$\hat{\boldsymbol{S}} = \mathrm{diag}(0, s_1, s_2, 0, s_4, 0, s_4, 0, s_4, s_9, s_{10}, s_9, s_{10}, s_{13}, s_{13}, s_{13}, s_{16}, s_{16}, s_{16}), \quad (16)$$

with $s_1 = 1.19$, $s_2 = s_{10} = 1.4$, $s_4 = 1.2$, $s_9 = s_{13} = 1/\tau$ and $s_{16} = 1.98$. The kinematic viscosity of the fluid is related to the relaxation time τ by $\nu = c_s^2(\tau - 1/2)\Delta t$, and pressure p is related to density by $p = \rho c_s^2$.

2.2. Interpolated bounceback scheme

The conventional no-slip boundary in LBM is based on the simple bounce-back scheme, which approximates the geometry in stair-case form. The effects of such an approximation are more pronounced at high Reynolds number, where the boundary layers are thinner, resulting in poor accuracy. In our simulations, we use a linearly interpolated bounce back scheme (Bouzidi et al., 2001) to accurately consider the curved geometry of the particle. A simplified one-dimensional interpolated bounce-back scheme is shown in figure 4. The parameter q_α is the fractional distance along the direction α of the fluid node to the actual wall and is given by $q_\alpha = |\boldsymbol{r}_w - \boldsymbol{r}_i|/|\boldsymbol{r}_b - \boldsymbol{r}_i|$.

Depending on whether $q_\alpha < 1/2$ or $q_\alpha \geq 1/2$, two different cases are to be considered:

$$f_{\bar{\alpha}}(\boldsymbol{r}_i, t) = 2q_\alpha \hat{f}_\alpha(\boldsymbol{r}_i, t) + (1 - 2q_\alpha)\hat{f}_\alpha(\boldsymbol{r}_j, t), \qquad q_\alpha < 1/2, \tag{17}$$

$$f_{\bar{\alpha}}(\boldsymbol{r}_i, t) = \frac{1}{2q_\alpha}\hat{f}_\alpha(\boldsymbol{r}_i, t) + \frac{(2q_\alpha - 1)}{2q_\alpha}\hat{f}_{\bar{\alpha}}(\boldsymbol{r}_i, t), \qquad q_\alpha \geq 1/2. \tag{18}$$

Here the subscript $\bar{\alpha}$ denotes the opposite direction of α. The notations $\hat{f}_\alpha$ and f_α denote the post-collision distribution functions before and after advection. From an implementation point of view, storing the distribution before and after advection ($\hat{f}_\alpha$ and f_α) results in additional memory burden. Therefore, Lallemand and Luo (2003) suggested to make use of the fact that advection is simply a spatial shifting of distributions, and that therefore the indices can be accordingly modified as

$$f_{\bar{\alpha}}(\boldsymbol{r}_i, t) = 2q_\alpha f_\alpha(\boldsymbol{r}_i + \boldsymbol{e}_\alpha \Delta t, t) + (1 - 2q_\alpha) f_\alpha(\boldsymbol{r}_i, t), \qquad q_\alpha < 1/2, \tag{19}$$

$$f_{\bar{\alpha}}(\boldsymbol{r}_i, t) = \frac{1}{2q_\alpha} f_\alpha(\boldsymbol{r}_i + \boldsymbol{e}_\alpha \Delta t, t) + \frac{(2q_\alpha - 1)}{2q_\alpha} f_{\bar{\alpha}}(\boldsymbol{r}_i - \boldsymbol{e}_\alpha \Delta t, t), \quad q_\alpha \geq 1/2. \tag{20}$$

The linear interpolation scheme was chosen for the no-slip boundary, as the parallel code requires only one layer of ghost cells as opposed to two layers in case of a quadratic scheme, resulting in additional communication overhead. Further, the improvement in solution accuracy is negligible between linear and quadratic interpolation schemes, provided sufficient resolution is used (Kruggel-Emden et al. (2016); Pan et al. (2006)). For the shapes considered - prolate & oblate ellipsoids and spherocylinder - the distance from fluid node to the wall boundary along the velocity directions are computed using ray-geometry intersection algorithms (Akenine-Möller et al., 2008). As ellipsoids can be described by a single equation, the ray-ellipsoid intersection is solved as a single problem. The ray-spherocylinder intersection is decomposed into three ray-intersection problems - (i) ray-cylinder and (ii) two ray-sphere intersection problems for the top and bottom hemispheres.

2.3. Boundary conditions and force evaluation

The schematic geometry of the domain is described in figure 5. A uniform velocity is prescribed at the inlet based on Hecht and Harting (2010), which

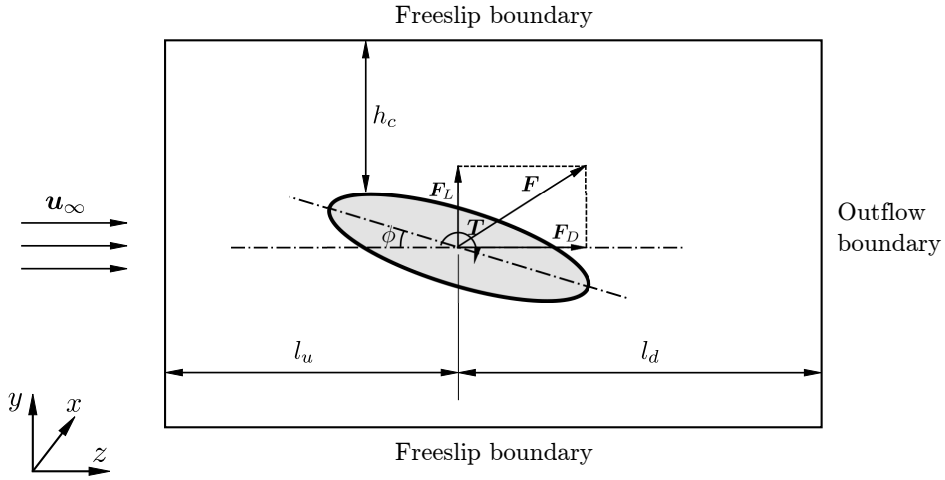

Figure 5: Simulation domain, the forces and torque acting on the particle and the boundary conditions.

extends the Zou and He boundary condition (Zou and He, 1997) to a D3Q19 lattice. The side walls are prescribed as free-slip boundary rather than as periodic boundary condition, which could cause the flow to deflect either up or down based on inclination of the non-spherical particle (Hölzer and Sommerfeld, 2009). The downstream (outlet) is specified by an axial-stress-free boundary condition with $\partial u_z/\partial z = 0$ (Aidun et al., 1998). All the simulations are initialized with uniform inlet velocity in the domain. The momentum contribution along a single fluid-solid link exerted on the particle by the fluid is computed using the momentum exchange method (Bouzidi et al., 2001; Mei et al., 2002; Lallemand and Luo, 2003) as

$$\boldsymbol{p}_\alpha(\boldsymbol{r}_b, t) = \boldsymbol{e}_\alpha(f_\alpha(\boldsymbol{r}_b, t) + f_{\overline{\alpha}}(\boldsymbol{r}_i, t)). \tag{21}$$

Correspondingly, the force and torque are computed as

$$\boldsymbol{F} = \sum_{\text{all } \boldsymbol{r}_b} \sum_{\alpha \neq 19} \boldsymbol{p}_\alpha(\boldsymbol{r}_b, t) \tag{22}$$

$$\boldsymbol{T} = \sum_{\text{all } \boldsymbol{r}_b} \sum_{\alpha \neq 19} (\boldsymbol{r}_w - \boldsymbol{r}_c) \times \boldsymbol{p}_\alpha(\boldsymbol{r}_b, t). \tag{23}$$

Here $\boldsymbol{r}_c$ is the center of gravity of the particle.

2.4. Grid resolution and domain independence study

Before proceeding to the simulations of non-spherical particles, the influence of grid resolution and domain size at different Re are assessed. The

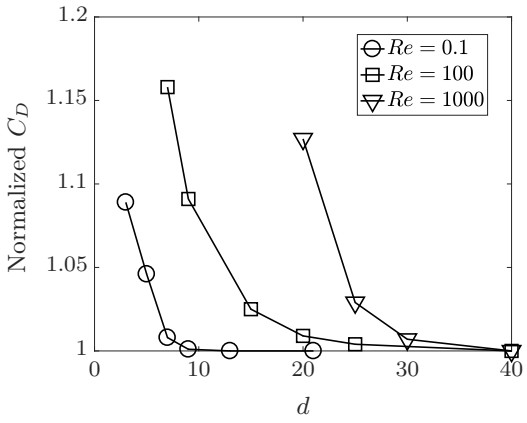

Figure 6: Normalized drag coefficient C_D of a sphere as function of particle resolution in diameter d (in lattice cells) for different Re.

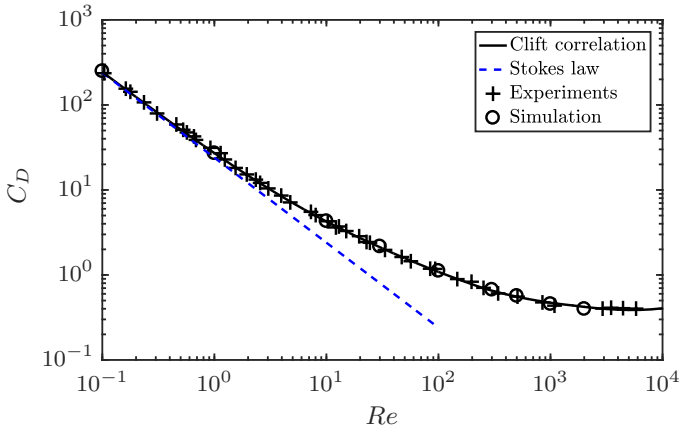

Figure 7: C_D at different Re for flow around sphere.

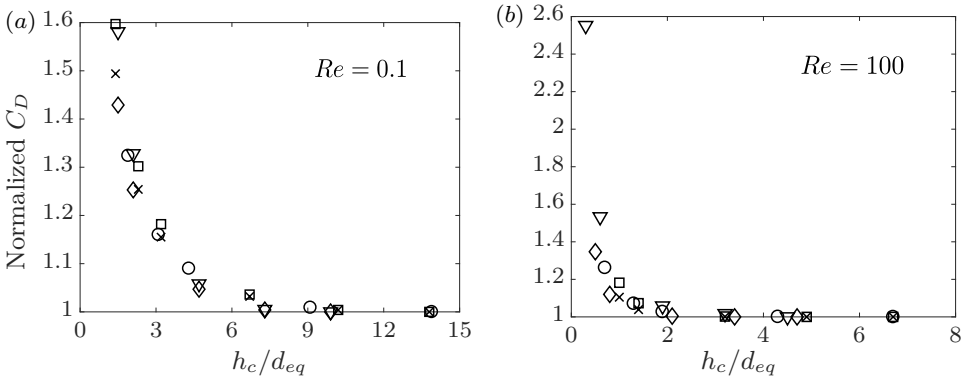

Figure 8: Influence of the clearance for (*a*) $Re = 0.1$ and (*b*) $Re = 100$. (○) sphere, ellipsoid 1 at (×) $\phi = 0°$ and (□) $\phi = 90°$, ellipsoid 2 at (◊) $\phi = 0°$ and (▽) $\phi = 90°$.

influence of grid resolution is tested with flow around an isolated sphere. The normalized C_D for different Re is plotted in figure 6. The normalization is done using the highest resolution C_D and not against any popularly available C_D correlations for a sphere. This is because at high Re, the C_D value becomes smaller and the available correlations themselves have minor deviations compared to the true C_D. This would be amplified strongly for small C_D values and therefore are not the best choice. Three different regimes are tested: (i) Stokes flow, (ii) intermediate Reynolds number at $Re = 100$ with a steady wake, and (iii) high Reynolds number $Re = 1000$ exhibiting complex, unsteady wake behind the sphere (in which case the mean C_D is reported). The influence of grid resolution is stronger with increasing Re, as seen in figure 6. For $Re = 1000$, we observe $C_D = 0.456$ at resolution $d_{eq} = 40$, which is in good agreement with the literature result, $C_D = 0.464$ from Vakarelski et al. (2016). The absolute C_D values for flow around sphere at different Re from our simulations are given in figure 7 along with the Clift correlation. It can be observed that there is good match from our results compared with the Clift correlation and also the experimental results at different Re.

The influence of the presence of side walls (confinement effect) is tested as a function of h_c/d_{eq}, where h_c is the clearance between the particle and the side walls (see figure 5), which is kept the same for the four lateral walls for a particular Re. Tests are performed for a sphere, ellipsoid 1 and ellipsoid 2 for $Re = 0.1$ and $Re = 100$. It can be observed from figure 8 that all the different geometries have consistent confinement effects for different Re, provided the clearance h_c is used to characterize confinement rather than particle center

	d_{min}					
Re	Ellipsoid 1	Ellipsoid 2	Fibre	h_c/d_{eq}	l_u/d_{eq}	l_d/d_{eq}
$0.1 \leq Re < 10$	16	16	16	10	10	10
$10 \leq Re \leq 100$	20	20	20	7	7.5	7.5
300	30	20	20	5	5	10
$1000, 2000$	40	30	30	4.5	5	10

Table 1: Details of the particle resolution in lattice cells and domain sizes at different Re. d_{min} is the minimum thickness of the particle.

to wall distance. As observed, between $Re = 0.1$ and $Re = 100$, the wall effects tend to become weaker for increasing Re and therefore confinement tests for $Re > 100$ are not presented here. For simulations with $Re > 100$, random confinement tests are performed and also literature data (Zastawny et al., 2012) are used for selecting appropriate h_c. It has been observed that $h_c \geq 4.5$ is sufficient to produce confinement independent results, as the viscous effects get weaker for increasing Re. Therefore, we maintained at least $h_c = 4.5$ for $Re > 100$.

Different simulations have different particle resolutions, upstream length l_u, downstream length l_d, and clearance h_c, depending on the Re. An extensive study regarding the upstream and downstream lengths is avoided to simplify the parameter space. Again, we have examined different literature containing flows around particles regarding the domain lengths (Zastawny et al., 2012; Hölzer and Sommerfeld, 2009). With this information, we have selected the upstream and downstream lengths. From our experience, only the downstream length is found to be significantly influencing results, specifically at high Re. Therefore, we have kept downstream length sufficiently long with $l_d/d_{eq} = 10$ for $Re \geq 300$ to avoid any influence of outflow boundary on the particle wake.

The influence of particle resolution (see figure 6) and the effects of domain size (see figure 8) at different Re are considered carefully on choosing the particle sizes. The chosen particle resolutions and the simulation domain sizes are listed in table 1. It has to be noted that the listed resolutions are the least thickness (d_{min}) of the particle. The other dimensions are always larger than d_{min} and therefore a good particle resolution is ensured. Since the grid independence study is performed prior to the actual simulations, the

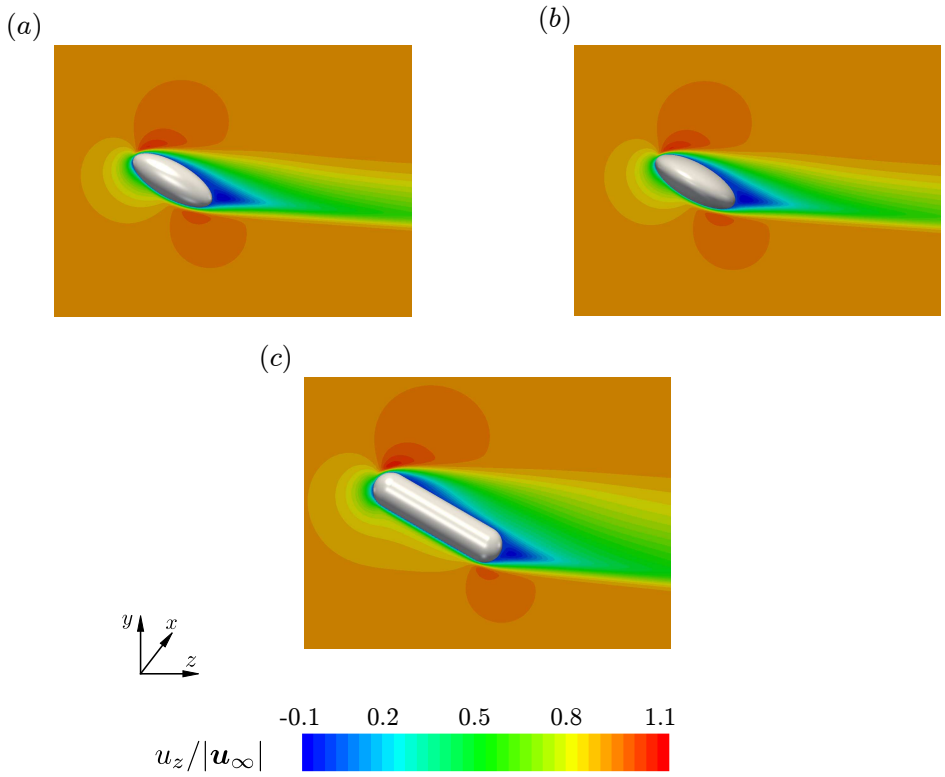

Figure 9: Velocity contours for flow around different particles at $Re = 300$ and $\phi = 30°$: (a) ellipsoid 1, (b) ellipsoid 2, and (c) fibre.

particle resolution is chosen such that the deviations are less than 3% of the true value.

3. Flow around various non-spherical particles

Detailed LBM simulations of the flow around 3 different non-spherical particles are performed. The simulated range of Reynolds number is $0.1 \leq Re \leq 2000$ at incident angles $0° \leq \phi \leq 90°$. As an example, the flow around different particles at $Re = 300$ and $\phi = 30°$ is shown in figure 9. Apart from producing accurate results through the simulations, fitting the observed data to a custom function, which has the least relative deviation is itself a challenge. As we will discuss, the functional form of the correlation should have relevant physical backing to produce the best fit and also to be applicable to extended Re ranges. We considered the physics carefully while

proposing the functional forms. The magnitude of the relative deviation between the correlation and simulation data is globally minimized using a Python optimization function. We used Powell's method (Powell, 1964), which was found to be best among the available optimization methods for our data.

3.1. Drag

We simulated different non-spherical particles at different incident angles ϕ and Re. The resulting C_D at different ϕ for various Re are plotted in figure 10. It can be noted that the exponent of the $\sin(\phi)$ term in the fits of C_D in Zastawny et al. (2012) are very close to 2 (see table 2 in Zastawny et al. (2012)). The same has been observed by Ouchene et al. (2016) for different prolate spheroids of aspect ratios upto 32. It might be tempting to relate this finding to a similar correlation expected in the Stokes flow for non-spherical particles. We have investigated this sine-squared behaviour for different non-spherical particles, both in the Stokes limit and at Re as high as 2000 (Sanjeevi and Padding, 2017). Surprisingly, the tested non-spherical particles exhibited *sine-squared* dependence of the mean C_D, even for complex unsteady flows at $Re = 2000$. We found that the linearity assumption, the reason for the sine-squared behaviour in the Stokes regime, does not hold at high Re, as may have been expected due to the flow non-linearities occurring at high Re. Rather, we find that the pressure distribution along the particle surface for different ϕ scales in a particular pattern. The pattern is dependent on the angle between the particle's surface-normal and the direction of the incident flow. This leads to the observed near *sine-squared* phenomenon. The phenomenon is found to be primarily holding for different elongated particles such as prolate spheroids, spherocylinders as well as low aspect ratio oblate spheroids. Flatter, high aspect ratio oblate spheroids do not exhibit the sine-squared dependence for reasons discussed in Sanjeevi and Padding (2017).

Initially, we considered the use of correlations similar to the popularly available Zastawny et al. (2012) form, since their form is quite flexible to capture the dependencies of C_D on Re and ϕ. Since the Re range is much larger in our case, with $0.1 \leq Re \leq 2000$ compared to $0.1 \leq Re \leq 300$ studied by Zastawny et al. (2012), our proposed correlations require further modifications. For reasons mentioned already, our proposed form takes an exponent 2 for the sine-term. We correlate the measured C_D at different Re

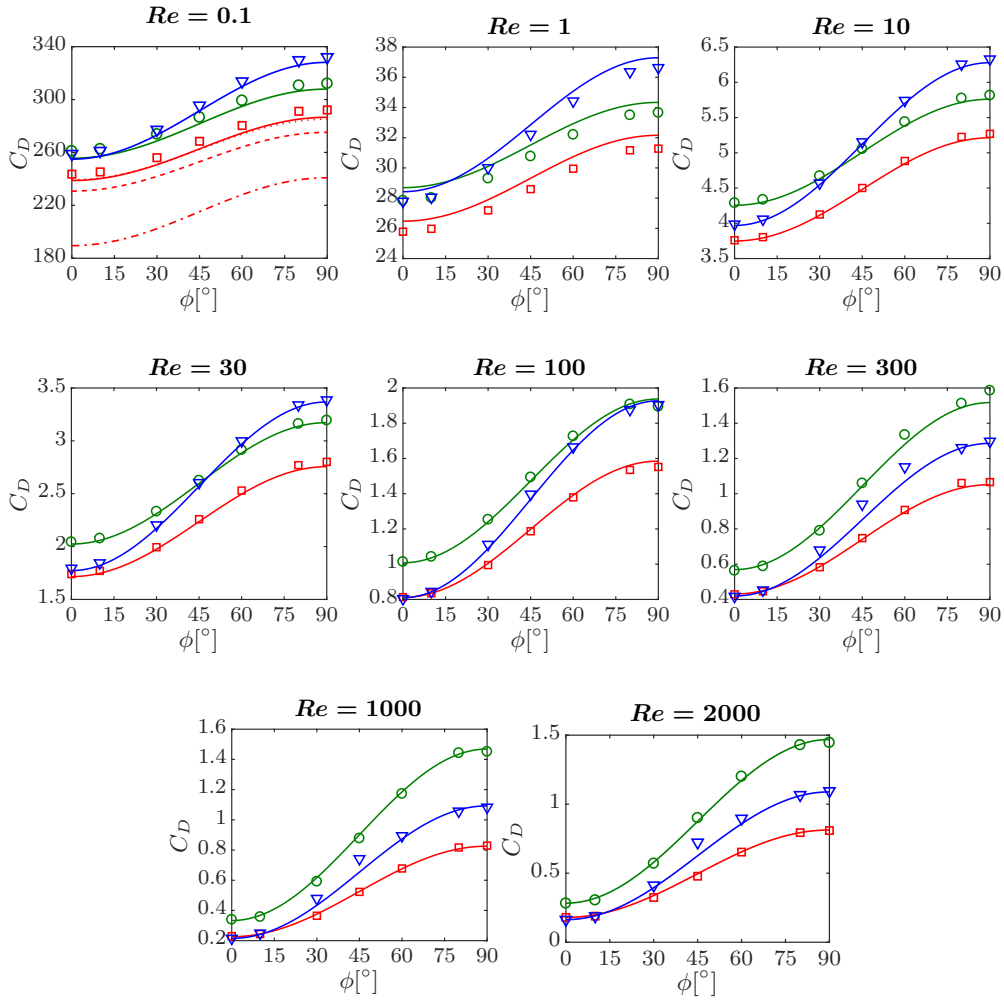

Figure 10: C_D vs ϕ at different Re for ellipsoid 1 (□), ellipsoid 2 (○), and fibre (▽). The corresponding solid lines in respective colors indicate the fit. At $Re = 0.1$ for ellipsoid 1, the dashed line corresponds to theory (Happel and Brenner, 1983), dashed-dot line for Zastawny et al. (2012) and dotted lines for Ouchene et al. (2016).

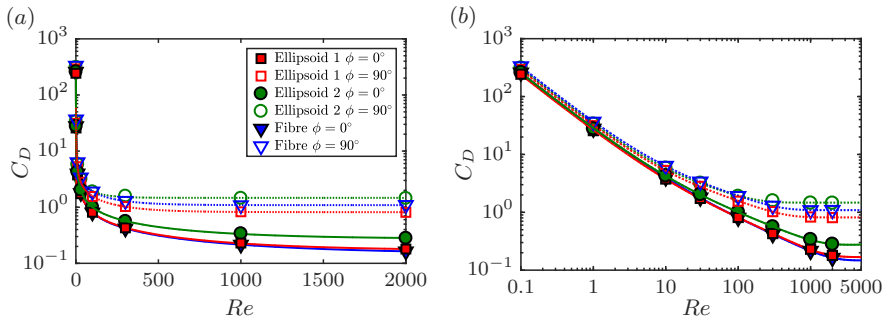

Figure 11: C_D against Re for different non-spherical particles with Re in (a) linear scale and (b) log-scale. The corresponding C_D correlations fit at $\phi = 0°$ (solid lines) and $\phi = 90°$ (dotted lines) are also shown.

	Ellipsoid 1		Ellipsoid 2		Fibre	
	$\phi = 0°$	$\phi = 90°$	$\phi = 0°$	$\phi = 90°$	$\phi = 0°$	$\phi = 90°$
a_1	23.10	27.93	24.66	30.18	24.48	31.89
a_2	3.397	4.286	4.059	4.396	3.965	5.519
a_3	0.364	0.234	0.349	0.156	0.41	0.229
a_4	0.0008	0.0018	0.0007	0.0073	0.0005	0.0032
a_5	0.169	0.815	0.278	1.469	0.15	1.089

Table 2: Coefficients for the C_D correlation.

and ϕ for the different tested non-spherical particles in the following form:

$$C_{D,\phi} = C_{D,\phi=0°} + (C_{D,\phi=90°} - C_{D,\phi=0°}) \sin^2 \phi \tag{24}$$

with

$$C_{D,\phi=0°,90°} = \left(\frac{a_1}{Re} + \frac{a_2}{Re^{a_3}}\right) e^{-a_4 Re} + a_5(1 - e^{-a_4 Re}) \tag{25}$$

The coefficients for the C_D correlation at 0° and 90° incident angle are listed in table 2. The table values close to 0 should not be ignored as they have a strong influence at high Re. Physically, the C_D should exhibit $1/Re$ scaling at Stokes flow, irrespective of the particle shape. In our form, the term a_1/Re replicates this behaviour. For intermediate Re, the term a_2/Re^{a_3} is dominant. Additionally, it is known that for a sphere, the C_D decays to a near constant value at large $Re > 10^3$ (see figure 7). Similar behaviour is observed for the different tested non-spherical particles and the term a_5

	Ellipsoid 1	Ellipsoid 2	Fibre
Mean(%)	1.48	1.66	2.18
Max.(%)	5.23	4.52	13.38

Table 3: Relative deviation between C_D results and the correlation.

captures the near constant C_D at high Re (see figure 11). Appropriately, the factors $e^{-a_4 Re}$ and $1 - e^{-a_4 Re}$ act as a smooth switch between these moderate and high Re regimes. Figure 11 shows the C_D values at $\phi = 0^\circ$ and $\phi = 90^\circ$ for different Re. With the proposed functional form for the correlation, the decay rate of C_D with respect to Re is captured well and therefore, we suggest that the C_D correlation can be extended to much lower Re in the Stokes regime and also to a few thousand Re magnitude greater than our simulations. To demonstrate this, figure 11(b) is shown with the fit from equation 25 upto $Re = 5000$ and it can observed that the trends are captured well for Re greater than the simulated limit of $Re = 2000$. Further, we show that the proposed C_D correlations are very accurate with respect to the measured coefficients and the same can be observed from figure 10. The mean and the maximum of the deviations between the C_D correlations and the actual results are listed in table 3. It can be observed that the mean of the absolute deviations are around 2% or less.

For creeping flows, it is known that the viscous forces dominate and the viscous forces themselves are dependent on the surface area of the particle. Conversely, for high Re, the pressure forces dominate and the pressure forces themselves are predominantly dependent on the projected surface area against the oncoming flow. This can also be observed in our simulations on comparison of C_D at $Re = 0.1$ and $Re = 2000$ in figure 10. For $Re = 0.1$, it is seen that the C_D of the fibre at different ϕ is at least equal or greater than that of disc-like ellipsoid 2. However at $Re = 2000$, we observe that the disc-like ellipsoid 2 has C_D values larger than that of the fibre.

3.1.1. Steady and unsteady regimes

The triggering of unsteady behaviour from a steady flow regime for a non-spherical particle depends not only on the Re but also on the incident angle ϕ. For a 6:1 prolate spheroid, Jiang et al. (2014) investigated the flow at a specific inclination of $\phi = 45^\circ$ at approximately $Re = 91, 363,$ and 1817 ($Re_d = 50, 200,$ and 1000 respectively). They report that even at $Re = 1817$,

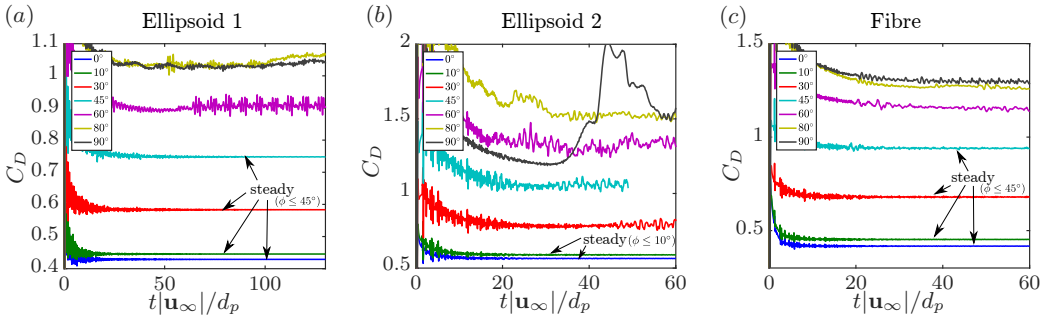

Figure 12: Time dependent behaviour of C_D at different incident angles ϕ at $Re = 300$ for (a) ellipsoid 1, (b) ellipsoid 2 and (c) fibre.

the flow exhibits predominantly steady and symmetric behaviour with the measured force coefficients exhibiting steady behaviour, with a mention that the flow field is on the verge of exhibiting vortex shedding behaviour for higher Re. These results are contrasting with the work of El Khoury et al. (2012) where the same prolate spheroid of ratio 6:1 is investigated at $91 \leq Re \leq 545$ ($50 \leq Re_d \leq 300$ respectively), but at cross-flow with $\phi = 90°$. They observe that unsteady behaviour is triggered at Reynolds numbers as low as $Re \approx 182$ ($Re_d = 100$). Therefore, we can say that the incident angle ϕ plays a major role in triggering unsteadiness. The simulations are run for a sufficiently large time $t_* = |\boldsymbol{u}_\infty|t/d_{eq}$, specifically for Re expected to exhibit unsteady regimes.

At $Re \leq 100$, all three tested particles show steady flow behaviour for all ϕ. However at $Re = 300$, the particles show unsteady behaviour for certain angles. Figure 12 shows the time-dependent drag of different non-spherical particles at $Re = 300$. It can be observed that the ellipsoid 1 and the fibre, both slender objects, exhibit steady behaviour for $\phi \leq 45°$ and unsteady behaviour for higher ϕ. However, the disc-like ellipsoid 2 exhibits steady behaviour only for low incident angles, i.e. $\phi \leq 10°$ and unsteady behaviour at higher incident angles. At higher $Re = 1000$, both the ellipsoid 1 and the fibre exhibit steady behaviour until $\phi \leq 10°$ and ellipsoid 2 exhibits unsteady behaviour for all ϕ. At $Re = 2000$, all particles exhibit unsteady behaviour for all incident angles ϕ, except for the fibre at $\phi = 0°$.

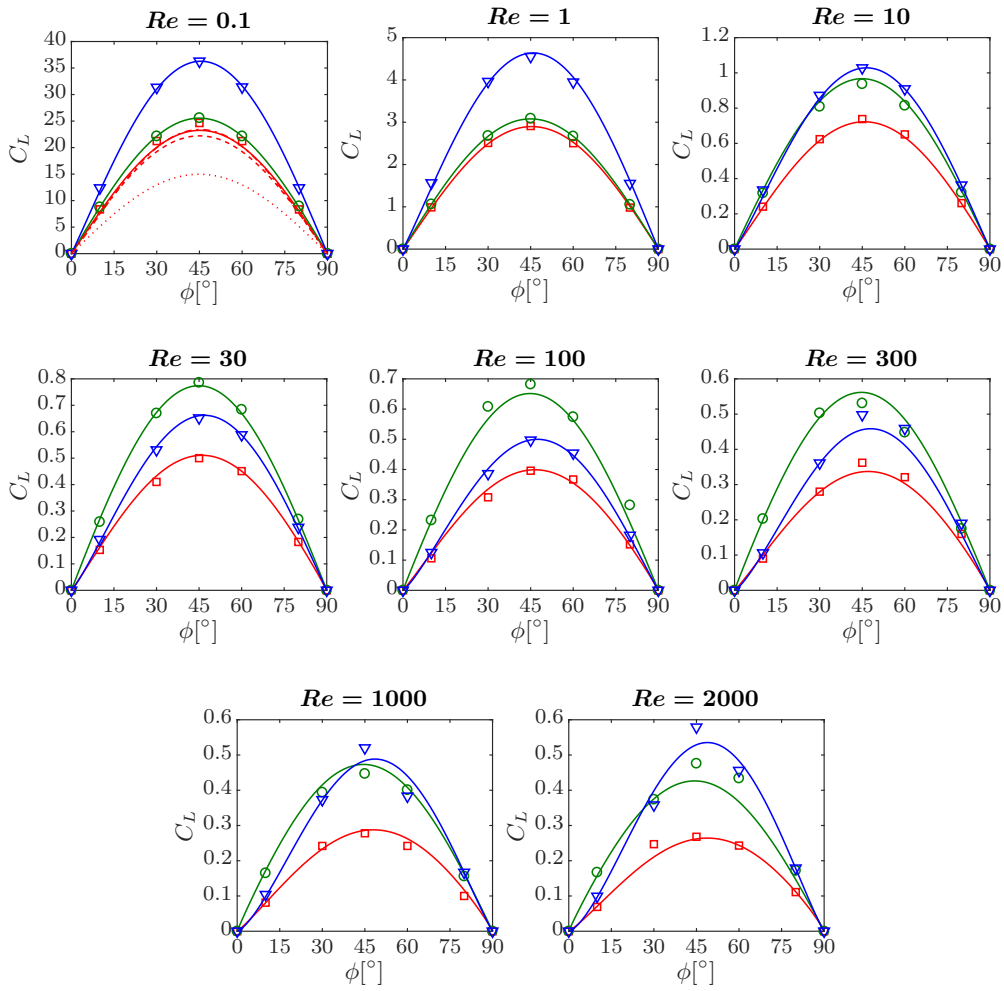

Figure 13: C_L vs ϕ at different Re for ellipsoid 1 (□), ellipsoid 2 (○), and fibre (▽). The corresponding solid lines in respective colors indicate the fit. At $Re = 0.1$ for ellipsoid 1, the dashed line corresponds to theory (Happel and Brenner, 1983), dashed-dot line for Zastawny et al. (2012) and dotted lines for Ouchene et al. (2016).

3.2. Lift

The lift coefficients C_L of the different tested particles and the corresponding correlation fits are plotted in figure 13. The proposed C_L fit takes the following form

$$C_{L,\phi} = \left(\frac{b_1}{Re} + \frac{b_2}{Re^{b_3}} + \frac{b_4}{Re^{b_5}} \right) \sin \phi^{(1+b_6 Re^{b_7})} \cos \phi^{(1+b_8 Re^{b_9})} \tag{26}$$

with the coefficients listed in table 4. The proposed C_L correlation form has both sine and cosine terms approaching exponent 1 for low Re, because this is the exact physical limit for Stokes flow (Happel and Brenner, 1983). As equation 6 is valid for Stokes flow, the corresponding $1/Re$ term of the C_L fit is dependent on the C_D, i.e. $b_1 \approx a_1(\phi = 90^\circ) - a_1(\phi = 0^\circ)$.

The mean and the maximum of the deviations between the C_L results and the fit are listed in table 5. The proposed correlation fits the observed results with good agreement with around 3-4% mean deviation. It is difficult in general to achieve a better fit due to the fact that the order of magnitudes of C_L are smaller than C_D and any small deviation is amplified. There is also a trend reversal in the skewness of the C_L vs ϕ curve for increasing Re. At Stokes flow, the C_L at different ϕ is symmetric. With increasing Re, up to the steady limits i.e. around $Re = 300$, the distribution skews to a particular direction and upon onset of unsteady behaviour, the skewness changes direction. This is observed for ellipsoid 1 and ellipsoid 2. Ellipsoid 1 results skew to the right upto $Re = 300$ and to the left for higher Re and vice versa for ellipsoid 2.

In general, the maximum C_L generated at a given Re is a function of the particle aspect ratio itself and also of the projected area of the particle at $\phi = 45^\circ$. For the same reason, even though both ellipsoids 1 and 2 are of same aspect ratio, the disc-like ellipsoid 2 always experiences more lift than the needle-like ellipsoid 1. Interestingly the fibre, which has aspect ratio 4, experiences the highest lift both in the Stokes regime and at $Re = 2000$ among the 3 tested particles. However at intermediate $Re = 100$, the disc-like ellipsoid 2 experiences maximum lift until the Re corresponding to onset of the unsteady flow. This is due to the fact that at intermediate Re, the disc-like ellipsoid 2 experiences stronger wake (compared to an elongated ellipsoid) at intermediate angles and this increases C_L directly. By stronger wake, we imply that the wake size is large and proportional to the projected area of the particle against the flow. Another interesting observation is that

	Ellipsoid 1	Ellipsoid 2	Fibre
b_1	4.484	5.28	6.83
b_2	1.326	8.96	0.071
b_3	0.122	0.234	−0.352
b_4	0	−8.095	2.592
b_5	0	0.325	0.298
b_6	0.016	−0.004	0.065
b_7	0.286	0.352	0.262
b_8	−0.010	−0.002	0.003
b_9	0.332	0.273	0.491

Table 4: Coefficients for the C_L correlation. The near zero coefficients should not be ignored as they would influence C_L at high Re.

	Ellipsoid 1	Ellipsoid 2	Fibre
Mean(%)	3.73	3.50	3.60
Max.(%)	18.54	20.86	15.74

Table 5: Relative deviation between C_L results and the correlation. It should be noted that the maximum relative deviations are observed at incident angles ϕ with C_L close to zero, i.e. ϕ near 0° and 90°.

the maximum C_L of the fibre monotonously reduces with increasing Re like other non-spherical particles. However after a critical Re, the trend reverses and the maximum C_L starts to increase again compared to other particles (see figure 13).

Even though equation 6 is only valid in the Stokes regime, we find that the same equation can be used as a reasonable approximation at higher Re, *specifically* for smooth, elongated particles. Examples of smooth, elongated particles include prolate spheroids, spherocylindrical capsules, etc. Sufficient care has to be exercised on applying equation 6 to shapes such as simple cylinders due to their sharp edges, as sharp edges might affect flow pattern and evolution of the instabilities significantly. However for high aspect ratio elongated cylinders, the influence of these sharp edges would be relatively weak compared to the frontal projected area of the particle for different ϕ. Equation 6 has been tested by us for different slender particles such as the prolate spheroids of different aspect ratios upto $Re = 2000$ (Sanjeevi

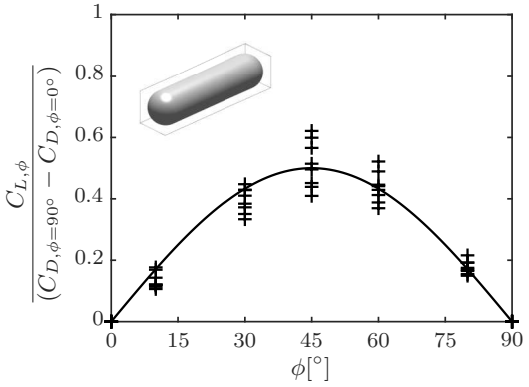

Figure 14: The normalized lift coefficient $C_{L,\phi}/(C_{D,\phi=90^\circ} - C_{D,\phi=0^\circ})$ for the fibre plotted against ϕ for different Re from 0.1 up to 2000. The solid line indicates $\sin\phi\cos\phi$. It should be noted that the used C_D and C_L values are from the simulations and not from the correlations.

and Padding, 2017). The mean of deviations between the simulations and equation 6 is under 15%. In this work, we also show that equation 6 can also be used for spherocylinders (fibres) as a decent approximation. Figure 14 shows the distribution of normalized C_L for the fibre at different Re upto 2000.

At the same time, it is interesting to note that a similar observation does not hold for disc-like oblate spheroids. Ellipsoid 2 in this work tested for $Re \leq 2000$ does not exhibit this behaviour. Another, flatter oblate spheroid of aspect ratio 4 has been tested by us at $Re = 100$ (Sanjeevi and Padding, 2017). The same oblate spheroid also does not exhibit the reasonable approximation of equation 6. The disc-like spheroids in general experience stronger wake compared to needle-like spheroids at Re beyond the Stokes regime. The stronger wake translates to larger lift at intermediate incident angles ϕ and thereby making the deviation larger for oblate spheroids (Sanjeevi and Padding, 2017). However in the absence of complete C_L data, equation 6 could still be used for oblate spheroids as an approximation.

3.2.1. Torque

Any non-spherical particle inclined with respect to a homogeneous flow also experiences a pitching torque. The torque coefficient C_T from the simulations and the correlation fits are plotted in figure 15. For Stokes flow, the pitching torque is known to vanish. Therefore, the Stokes regime C_T results are ignored while making the fit. The proposed C_T correlation fitted for the

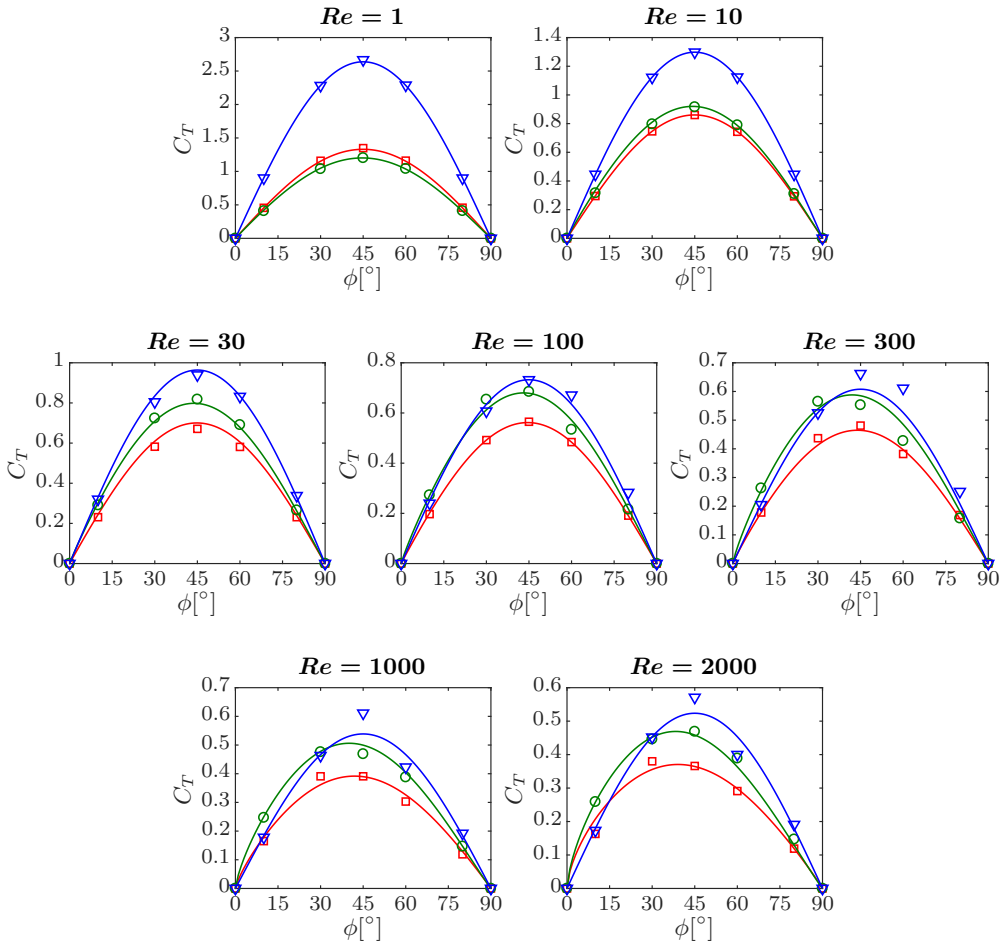

Figure 15: C_T vs ϕ at different Re for ellipsoid 1 (□), ellipsoid 2 (○), and fibre (▽). It has to be noted that torque vanishes in Stokes flow and therefore ignored for the correlation.

	Ellipsoid 1	Ellipsoid 2	Fibre
c_1	2.660	3.643	5.079
c_2	0.190	0.178	0.342
c_3	0	-1.252	0.197
c_4	0	0.319	-0.161
c_5	-8.73×10^{-4}	-0.018	0
c_6	0.798	0.387	0
c_7	-3.70×10^{-5}	0.004	0
c_8	0.963	0.349	0

Table 6: Coefficients for the C_T correlation. The near zero coefficients should not be ignored as they would influence C_T at high Re.

	Ellipsoid 1	Ellipsoid 2	Fibre
Mean(%)	3.40	3.43	4.12
Max.(%)	27.30	15.13	17.18

Table 7: Relative deviation between C_T results and the correlation. The maximum relative deviations are observed at incident angles ϕ with C_T close to zero, i.e., near 0° and 90°.

range $1 \leq Re \leq 2000$ takes the following form

$$C_{T,\phi} = \left(\frac{c_1}{Re^{c_2}} + \frac{c_3}{Re^{c_4}} \right) \sin \phi^{(1+c_5 Re^{c_6})} \cos \phi^{(1+c_7 Re^{c_8})} \tag{27}$$

with coefficients listed in table 6. Similar to C_L, the C_T values exhibit near symmetric behaviour and vanish to zero at the extreme incident angles ϕ and therefore, the fitted correlation is very sensitive to minor deviations. The mean and maximum deviations of the correlation for the different tested particles are listed in table 7. Even though good agreements are observed in figure 15, the overall mean relative deviation is around 3.5%. This mainly stems from larger relative deviations for the near-zero C_T values observed close to $\phi = 0^\circ$ and $\phi = 90^\circ$.

4. Comparison with literature correlations

In this section, we compare our simulation results with different correlations available in the literature. Hölzer and Sommerfeld (2008) provide only

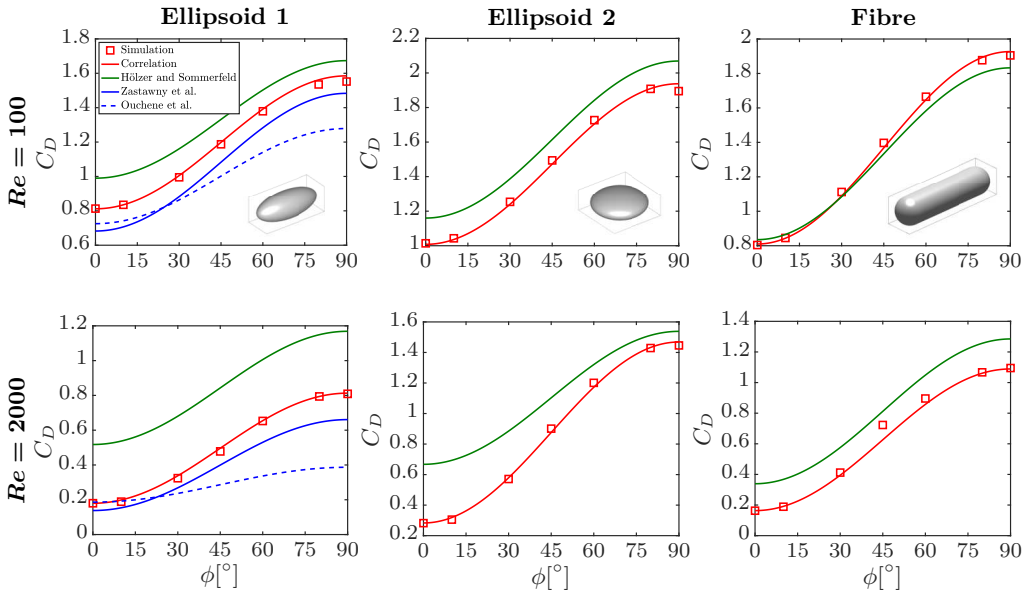

Figure 16: Comparison of C_D results with literature correlations.

a C_D correlation, but it is applicable to arbitrary non-spherical particles. We use it at $\phi = 0°, 90°$ and interpolate for intermediate incident angles ϕ using equation 24 as all tested particles exhibit near sine-squared C_D behaviour for all Re. Zastawny et al. (2012) and Ouchene et al. (2016) provide C_D, C_L and C_T for specific non-spherical particles limited to steady flows. The provided correlations have different decay rates for different Re regimes. If such decay rates are captured accurately, it is possible that their correlations can be extended to ranges beyond their tested limits. It is shown in figure 1 that the fluidized particles experience flows upto $Re = 2000$. In this section, we therefore test the correlations of both Zastawny et al. (2012) and Ouchene et al. (2016) upto $Re = 2000$, even though their tested Re regime is roughly an order of 10 less. Two cases are considered, one at $Re = 100$ and another at $Re = 2000$ and the corresponding drag, lift and torque coefficients are compared. At the moment of writing, we are not able to reproduce the C_D and C_L correlation results available in Ouchene et al. (2016) due to typographical errors in their published correlation. The corresponding typographical corrections have been communicated to us by Ouchene et al. (2016).

The C_D comparisons for the different non-spherical particles are shown in figure 16. For ellipsoid 1, we observe that our C_D results are in good

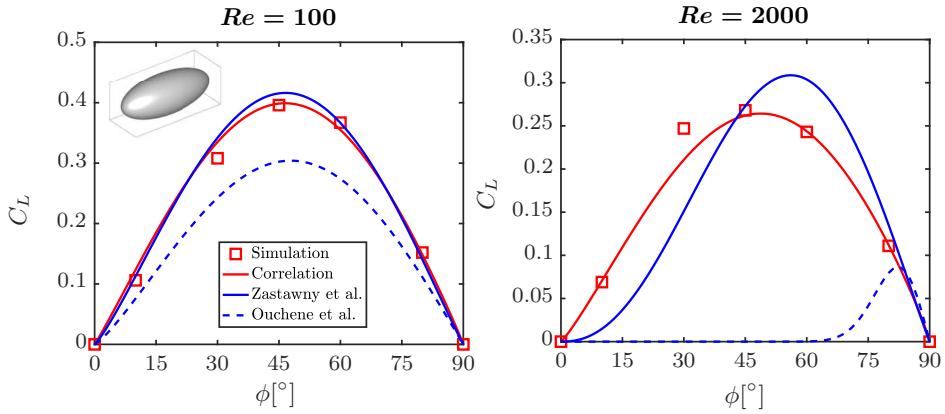

Figure 17: Comparison of C_L results of ellipsoid 1 with literature correlations.

agreement with Zastawny et al. (2012) for both $Re = 100$ and $Re = 2000$, even though their correlation is valid only up to $Re = 300$. However, the results of Zastawny et al. (2012) are not accurate for Stokes flow as can be observed from figure 10 for $Re = 0.1$ on comparison with theoretical solutions and other literature results. This is primarily due to the fact that Zastawny et al. (2012) use a domain of $20d_{eq} \times 20d_{eq} \times 10d_{eq}$ for $Re < 1$. Their lowest domain dimension $10d_{eq}$ is not sufficient for Stokes flow, where viscous effects are dominant and thereby requiring larger domain size.

On the other hand, the more generic correlation of Ouchene et al. (2016) for different prolate spheroids is comparatively less accurate. While their $C_{D,\phi=0^\circ}$ is found to be sufficiently accurate, the $C_{D,\phi=90^\circ}$ is not accurate, thereby leading to an inaccurate prediction overall with increasing Re. We find that the Hölzer and Sommerfeld (2008) correlation works reasonably well for all the tested non-spherical particles at $Re = 100$ but not well for $Re = 2000$. This is due to the fact that their correlation is intended to be more generically applicable to all non-spherical particles and for a wide range of Re. Further, the C_D itself reduces with increasing Re, with a rate that depends on the particle geometry. Therefore at high Re, any deviation is amplified due to the smaller C_D value.

The comparison of C_L values for ellipsoid 1 are given in figure 17. For $Re = 100$, we observe that our simulations results are in very good agreement with Zastawny et al. (2012). The results of Ouchene et al. (2016) exhibit large deviations, with a maximum deviation of around 40%. For $Re = 2000$, the results of Zastawny et al. (2012) are still reasonably accurate considering

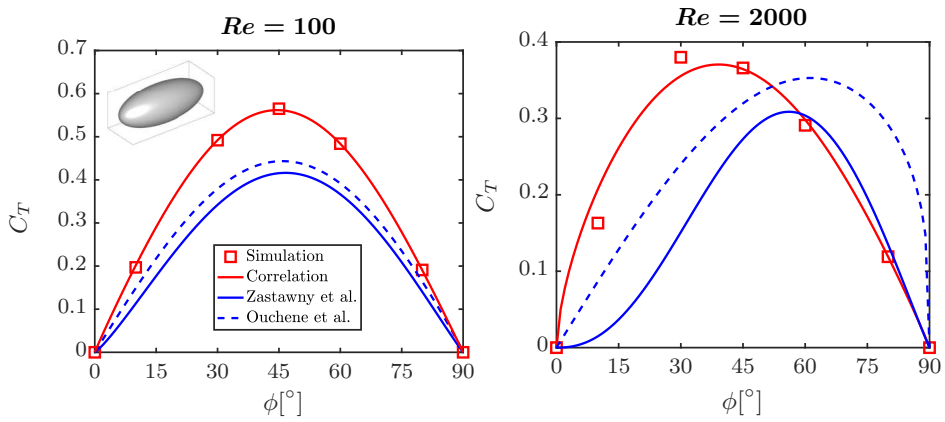

Figure 18: Comparison of C_T results of ellipsoid 1 with literature correlations.

their tested limit is $Re = 300$. However, the C_L correlation of Ouchene et al. (2016) performs poorly at $Re = 2000$. As discussed earlier for C_D, if the coefficient decay rates are captured with proper physical bounds, the Re limits can be extended much further. In a similar sense, the C_L correlation of Ouchene et al. (2016) does not capture the decay rates accurately and also their skewness term $\sin^{1.002^{Re}} \phi \cos \phi$ makes the C_L skewness extreme for higher Re.

Generally, determining the particle correlations involves a two-step process: (i) performing accurate simulations and (ii) fitting the simulation results in an accurate form. The work of Ouchene et al. (2016) is performed using Ansys Fluent, which is one of the most reliable commercial solvers and therefore, simulation accuracy is good. However, the choice of the fitting form is where most of the precision is lost, since the work of Ouchene et al. (2016) covers a wide range of aspect ratios, Re and incident angles. Even for a simple C_D correlation for a sphere, the accurate correlation forms (for example the Clift correlation) split the correlation into multiple Re range. For the same reason, we observe that C_D and C_L correlations of Ouchene et al. (2016) have poor accuracy (see figures 16 and 17) as they are done by a single fit. However, their C_T is found to be more accurate as it is split for two different aspect ratio ranges (see figure 18). Our work does not have this issue as the fits are independent for the different particles investigated and hence simpler.

Regarding C_T, the correlations of Zastawny et al. (2012) and Ouchene et al. (2016) are compared for ellipsoid 1 with our results in figure 18. We

observe that both the literature results are in good agreement with our simulation results for $Re = 100$. At $Re = 2000$, there is still a reasonable match on comparing the maximum amplitudes of the C_T, but slight variation in the skewness. Our C_T distribution is slightly skewed to the left and the literature results slightly to the right. This is again due to the fact that the literature results are only performed for predominantly steady flow regimes with $Re \leq 300$.

5. Conclusion

The flow around different non-spherical particles has been simulated using the MRT-LBM scheme for different incident angles ϕ. Interpolated bounce-back is used to achieve high accuracy compared to the conventional staircase no-slip boundaries in LBM, especially at high Re. The simulations have been performed from the Stokes limit to $Re = 2000$, while previous works were mainly limited to steady flows up to $Re = 300$. Different tests have been performed to assess the influence of grid resolution and also the size of the domain, thereby ensuring the quality of the results. The influence of the particle's geometry and also the incident angle ϕ has a significant effect on the onset of unsteady flow behaviour. We observed that the simulated particles exhibit sine-squared mean drag scaling with ϕ, starting from the Stokes limit and even upto $Re = 2000$. Such an agreement at high Re is not due to linearity of the flow fields as in Stokes flow, but rather due to consistent pressure pattern depending on local surface normal of the particle (Sanjeevi and Padding, 2017).

At the same time, we observed that the lift and torque coefficient display a symmetric behaviour at Stokes flow and a slightly skewed trend for larger Re. The onset of unsteady flow behaviour also influences the direction of the skewness i.e. different skewing directions before and after the transient Re for unsteady flow behaviour. Correlations for drag, lift and torque coefficients have been proposed, taking in consideration of known theoretical limits at low Re and different decay rates at high Re. This implies that our correlations can be extended to regimes beyond our tested limits, to lower Re in the Stokes regime and $Re > 2000$ to a considerable extent, especially the correlations of C_D and C_L. We also propose that in the absence of complete C_L data for intermediate incident angles ϕ, the C_L equation of the Stokes flow (equation 6) can be used as a reasonable approximation at high Re. Better agreement is observed for smooth, elongated particles such as prolate

(needle-like) spheroids and spherocylindrical fibres compared to oblate (disc-like) spheroids. The reason why disc-like spheroids show poor agreement is due to increased lift at intermediate incident angles ϕ due to stronger wake (Sanjeevi and Padding, 2017).

Good agreement between the measured data and the fits is observed, with deviations of around 2% for C_D and around 3.5% for C_L and C_T. The proposed correlations will greatly help Euler-Lagrangian simulations, catering the practical Re regimes observed in fluidized beds.

Acknowledgements

We thank the European Research Council for its financial support under its consolidator grant scheme, contract no. 615096 (NonSphereFlow). The work has been made possible by a grant for computation time, project number SH-351-15, financed by the Netherlands Organisation for Scientific Research (NWO). We thank Vinay Mahajan for providing simulation data for figure 1 and Barry Fitzgerald for a careful reading of the manuscript.

Appendix A.

The transformation matrix $\boldsymbol{M}$ used for transforming from velocity to moment space based on d'Humières et al. (2002) is

$$\boldsymbol{M} = \begin{pmatrix}
1 & 1 & 1 & 1 & 1 & 1 & 1 & 1 & 1 & 1 & 1 & 1 & 1 & 1 & 1 & 1 & 1 & 1 & 1 \\
-11 & -11 & -11 & -11 & -11 & -11 & 8 & 8 & 8 & 8 & 8 & 8 & 8 & 8 & 8 & 8 & 8 & 8 & -30 \\
-4 & -4 & -4 & -4 & -4 & -4 & 1 & 1 & 1 & 1 & 1 & 1 & 1 & 1 & 1 & 1 & 1 & 1 & 12 \\
1 & -1 & 0 & 0 & 0 & 0 & 1 & 1 & 1 & 1 & -1 & -1 & -1 & -1 & 0 & 0 & 0 & 0 & 0 \\
-4 & 4 & 0 & 0 & 0 & 0 & 1 & 1 & 1 & 1 & -1 & -1 & -1 & -1 & 0 & 0 & 0 & 0 & 0 \\
0 & 0 & 1 & -1 & 0 & 0 & 1 & -1 & 0 & 0 & 1 & -1 & 0 & 0 & 1 & 1 & -1 & -1 & 0 \\
0 & 0 & -4 & 4 & 0 & 0 & 1 & -1 & 0 & 0 & 1 & -1 & 0 & 0 & 1 & 1 & -1 & -1 & 0 \\
0 & 0 & 0 & 0 & 1 & -1 & 0 & 0 & 1 & -1 & 0 & 0 & 1 & -1 & 1 & -1 & 1 & -1 & 0 \\
0 & 0 & 0 & 0 & -4 & 4 & 0 & 0 & 1 & -1 & 0 & 0 & 1 & -1 & 1 & -1 & 1 & -1 & 0 \\
2 & 2 & -1 & -1 & -1 & -1 & 1 & 1 & 1 & 1 & 1 & 1 & 1 & 1 & -2 & -2 & -2 & -2 & 0 \\
-4 & -4 & 2 & 2 & 2 & 2 & 1 & 1 & 1 & 1 & 1 & 1 & 1 & 1 & -2 & -2 & -2 & -2 & 0 \\
0 & 0 & 1 & 1 & -1 & -1 & 1 & 1 & -1 & -1 & 1 & 1 & -1 & -1 & 0 & 0 & 0 & 0 & 0 \\
0 & 0 & -2 & -2 & 2 & 2 & 1 & 1 & -1 & -1 & 1 & 1 & -1 & -1 & 0 & 0 & 0 & 0 & 0 \\
0 & 0 & 0 & 0 & 0 & 0 & 1 & -1 & 0 & 0 & -1 & 1 & 0 & 0 & 0 & 0 & 0 & 0 & 0 \\
0 & 0 & 0 & 0 & 0 & 0 & 0 & 0 & 0 & 0 & 0 & 0 & 0 & 0 & 1 & -1 & -1 & 1 & 0 \\
0 & 0 & 0 & 0 & 0 & 0 & 0 & 0 & 1 & -1 & 0 & 0 & -1 & 1 & 0 & 0 & 0 & 0 & 0 \\
0 & 0 & 0 & 0 & 0 & 0 & 1 & 1 & -1 & -1 & -1 & -1 & 1 & 1 & 0 & 0 & 0 & 0 & 0 \\
0 & 0 & 0 & 0 & 0 & 0 & -1 & 1 & 0 & 0 & -1 & 1 & 0 & 0 & 1 & 1 & -1 & -1 & 0 \\
0 & 0 & 0 & 0 & 0 & 0 & 0 & 0 & 1 & -1 & 0 & 0 & 1 & -1 & -1 & 1 & -1 & 1 & 0
\end{pmatrix}.$$

References

Aidun, C. K., Lu, Y., Ding, E.-J., 1998. Direct analysis of particulate suspensions with inertia using the discrete Boltzmann equation. Journal of Fluid Mechanics 373 (1), 287–311.

Akenine-Möller, T., Haines, E., Hoffman, N., 2008. Real-time rendering. CRC Press.

Beetstra, R., Van der Hoef, M. A., Kuipers, J. A. M., 2007. Drag force of intermediate Reynolds number flow past mono-and bidisperse arrays of spheres. AIChE Journal 53 (2), 489–501.

Bouzidi, M., Firdaouss, M., Lallemand, P., 2001. Momentum transfer of a Boltzmann-lattice fluid with boundaries. Physics of Fluids (1994-present) 13 (11), 3452–3459.

d'Humières, D., Ginzburg, I., Krafczyk, M., Lallemand, P., Luo, L.-S., 2002. Multiple–relaxation–time lattice Boltzmann models in three dimensions. Philosophical Transactions of the Royal Society of London A: Mathematical, Physical and Engineering Sciences 360 (1792), 437–451.

Di Felice, R., 1994. The voidage function for fluid-particle interaction systems. International Journal of Multiphase Flow 20 (1), 153–159.

Eitel-Amor, G., Meinke, M., Schröder, W., 2013. A lattice-Boltzmann method with hierarchically refined meshes. Computers & Fluids 75, 127–139.

El Khoury, G. K., Andersson, H. I., Pettersen, B., 2012. Wakes behind a prolate spheroid in crossflow. Journal of Fluid Mechanics 701, 98–136.

Ganser, G. H., 1993. A rational approach to drag prediction of spherical and nonspherical particles. Powder Technology 77 (2), 143–152.

Haider, A., Levenspiel, O., 1989. Drag coefficient and terminal velocity of spherical and nonspherical particles. Powder technology 58 (1), 63–70.

Happel, J., Brenner, H., 1983. Low Reynolds number hydrodynamics: with special applications to particulate media. Vol. 1. Springer Science & Business Media.

He, X., Luo, L.-S., 1997. Lattice Boltzmann model for the incompressible Navier–Stokes equation. Journal of statistical Physics 88 (3-4), 927–944.

Hecht, M., Harting, J., 2010. Implementation of on-site velocity boundary conditions for D3Q19 lattice Boltzmann simulations. Journal of Statistical Mechanics: Theory and Experiment 2010 (01), P01018.

Hilton, J. E., Mason, L. R., Cleary, P. W., 2010. Dynamics of gas–solid fluidised beds with non-spherical particle geometry. Chemical Engineering Science 65 (5), 1584–1596.

Hölzer, A., Sommerfeld, M., 2008. New simple correlation formula for the drag coefficient of non-spherical particles. Powder Technology 184 (3), 361–365.

Hölzer, A., Sommerfeld, M., 2009. Lattice Boltzmann simulations to determine drag, lift and torque acting on non-spherical particles. Computers & Fluids 38 (3), 572–589.

Huang, H., Yang, X., Krafczyk, M., Lu, X.-Y., 2012. Rotation of spheroidal particles in Couette flows. Journal of Fluid Mechanics 692, 369–394.

Jeffery, G. B., 1922. The motion of ellipsoidal particles immersed in a viscous fluid. In: Proceedings of the Royal Society of London A: Mathematical, Physical and Engineering Sciences. Vol. 102. The Royal Society, pp. 161–179.

Jiang, F., Gallardo, J. P., Andersson, H. I., 2014. The laminar wake behind a 6: 1 prolate spheroid at 45 incidence angle. Physics of Fluids (1994-present) 26 (11), 113602.

Kruggel-Emden, H., Kravets, B., Suryanarayana, M. K., Jasevicius, R., 2016. Direct numerical simulation of coupled fluid flow and heat transfer for single particles and particle packings by a LBM-approach. Powder Technology 294, 236–251.

Ladd, A. J. C., 1994a. Numerical simulations of particulate suspensions via a discretized Boltzmann equation. Part 1. Theoretical foundation. Journal of Fluid Mechanics 271 (1), 285–309.

Ladd, A. J. C., 1994b. Numerical simulations of particulate suspensions via a discretized Boltzmann equation. Part 2. Numerical results. Journal of Fluid Mechanics 271, 311–339.

Ladd, A. J. C., Verberg, R., 2001. Lattice-Boltzmann simulations of particle-fluid suspensions. Journal of Statistical Physics 104 (5-6), 1191–1251.

Lallemand, P., Luo, L.-S., 2003. Lattice Boltzmann method for moving boundaries. Journal of Computational Physics 184 (2), 406–421.

Leith, D., 1987. Drag on nonspherical objects. Aerosol science and technology 6 (2), 153–161.

Mei, R., Yu, D., Shyy, W., Luo, L.-S., 2002. Force evaluation in the lattice Boltzmann method involving curved geometry. Physical Review E 65 (4), 041203.

Oberbeck, A., 1876. Über stationäre Flüssigkeitsbewegungen mit Berücksichtigung der inneren Reibung. Journal für die reine und angewandte Mathematik 81, 62–80.

Ouchene, R., Khalij, M., Arcen, B., Tanière, A., 2016. A new set of correlations of drag, lift and torque coefficients for non-spherical particles and large Reynolds numbers. Powder Technology 303, 33–43.

Ouchene, R., Khalij, M., Taniere, A., Arcen, B., 2015. Drag, lift and torque coefficients for ellipsoidal particles: From low to moderate particle reynolds numbers. Computers & Fluids 113, 53–64.

Pan, C., Luo, L.-S., Miller, C. T., 2006. An evaluation of lattice Boltzmann schemes for porous medium flow simulation. Computers & fluids 35 (8), 898–909.

Powell, M. J., 1964. An efficient method for finding the minimum of a function of several variables without calculating derivatives. The computer journal 7 (2), 155–162.

Richter, A., Nikrityuk, P. A., 2012. Drag forces and heat transfer coefficients for spherical, cuboidal and ellipsoidal particles in cross flow at sub-critical Reynolds numbers. International Journal of Heat and Mass Transfer 55 (4), 1343–1354.

Richter, A., Nikrityuk, P. A., 2013. New correlations for heat and fluid flow past ellipsoidal and cubic particles at different angles of attack. Powder technology 249, 463–474.

Rubinstein, G. J., Ozel, A., Yin, X., Derksen, J. J., Sundaresan, S., 2017. Lattice Boltzmann simulations of low-Reynolds-number flows past fluidized

spheres: effect of inhomogeneities on the drag force. Journal of Fluid Mechanics 833, 599–630.

Sanjeevi, S. K. P., Padding, J. T., 2017. On the orientational dependence of drag experienced by spheroids. Journal of Fluid Mechanics 820.

Vakarelski, I. U., Berry, J. D., Chan, D. Y. C., Thoroddsen, S. T., 2016. Leidenfrost vapor layers reduce drag without the crisis in high viscosity liquids. Physical Review Letters 117 (11), 114503.

Zastawny, M., Mallouppas, G., Zhao, F., Van Wachem, B., 2012. Derivation of drag and lift force and torque coefficients for non-spherical particles in flows. International Journal of Multiphase Flow 39, 227–239.

Zou, Q., He, X., 1997. On pressure and velocity boundary conditions for the lattice Boltzmann BGK model. Physics of Fluids (1994-present) 9 (6), 1591–1598.